# gwforge: A user-friendly package to generate gravitational-wave mock data

Koustav Chandra [1]

[1] *Institute for Gravitation & the Cosmos and Department of Physics, The Pennsylvania State University, University Park PA 16802, USA*

## ABSTRACT

The next-generation gravitational-wave detectors, with their improved sensitivity and wider frequency bandwidth, will be capable of observing almost every compact binary coalescence signal from epochs before the first stars began to form, increasing the number of detectable binaries to hundreds of thousands annually. This will enable us to observe compact objects through cosmic time, probe extreme matter phenomena, do precision cosmology, study gravity in strong field dynamical regimes and potentially allow observation of fundamental physics beyond the standard model. However, the richer data sets produced by these detectors will pose new computational, physical and astrophysical challenges, necessitating the development of novel algorithms and data analysis strategies. To aid in these efforts, this paper introduces gwforge, a user-friendly, lightweight PYTHON package, to generate mock data for next-generation detectors. We demonstrate the package's capabilities through data simulation examples and highlight a few potential applications: performance loss due to foreground noise, bright-siren cosmology and impact of waveform systematics on binary parameter estimation.

## 1. INTRODUCTION

The next-generation (XG) ground-based gravitational-wave (GW) detectors, such as the Cosmic Explorer (CE) and the Einstein Telescope (ET), promise to significantly improve both the detection horizon and the frequency bandwidth of observable compact binary coalescence (CBC) signals (Punturo et al. 2010; Reitze et al. 2019; Maggiore et al. 2020; Evans et al. 2021; Borhanian & Sathyaprakash 2022; Branchesi et al. 2023; Evans et al. 2023; Gupta et al. 2023). This expanded detection horizon will allow us to observe compact binary coalescence (CBC) signals from greater distances, thereby increasing the number of detectable binaries by several orders of magnitude. Additionally, the increased bandwidth of these detectors could allow for the observation of a CBC signal over durations spanning minutes to even hours (Regimbau et al. 2012; Evans et al. 2021; Gupta et al. 2023).

Given this, the XG GW detectors will have far-reaching scientific potential. However, the "richer" GW detector data will present computational, physical and astrophysical challenges. Existing GW analysis tools, waveform models and detector calibration techniques will be insufficient in XG era (Evans et al. 2021; Pizzati et al. 2022; Hu & Veitch 2023). Also, the sheer volume

of observed signals will necessitate the development of novel algorithms for detecting the signals and extracting the science out of them. It is, therefore, imperative to quantify the limitations of current tools when employed in XG data analysis.

To support this effort and ensure that XG detectors will achieve their scientific potential, it is crucial to generate playground datasets to allow the GW community to develop and tune their algorithms. Such an effort will drive the development of new data analysis strategies, such as faster search and parameter estimation (PE) techniques, improved waveform modelling, dealing with non-stationary noise and methods to identify subtle physical effects, such as finite size effects in neutron star (NS).

This paper introduces gwforge, a user-friendly PYTHON package to simulate the mock data for the proposed XG detectors based on our understanding of our universe. One primary reason for developing gwforge is the anticipated abundance of signals in XG data, necessitating systematic data generation that accounts for realistic population models and the complexities of overlapping signals. This code is built on existing GW packages, such as PYCBC, Bilby, gwpy and gwpopulation.

The subsequent sections of this paper are structured to highlight the user-friendly nature of the code. Sec 2 provides an overview of the code, including installation instructions in Sec. 2.1. Sec. 3 provides the necessary

Corresponding author: kbc595@psu.edu

theoretical background and an example to generate a day's worth of coloured Gaussian XG network data with CBC signals. Sec. 4 is devoted to a few studies one can do using the prepared dataset in the previous section, and we conclude in Sec. 5.

## 2. CODE OVERVIEW

### 2.1. *Installation*

The source code is available on the `git` repository (Chandra 2024a), which includes instructions for contributing to code development. Comprehensive documentation regarding installation, functionality, and user syntax is provided on the project's website (Chandra 2024b). Example setup scripts discussed in this work are available in the `git` repository.

### 2.2. *Packages*

At the top level, `gwforge` comprises three main packages: `population`, `ifo` and `inject`. The `population` package provides functions essential to generate individual compact binary properties $\boldsymbol{\theta}$ based on hyper-parameters $\boldsymbol{\Lambda}$ that describe the population characteristics. These characteristics are defined by phenomenological population models or detailed physical simulations, such as population synthesis or N-body dynamical simulations generated using population synthesis codes such as COMPAS (Stevenson et al. 2017; Vigna-Gómez et al. 2018). `gwforge` integrates all phenomenological population models from `gwpopulation` and includes additional distribution functions such as a `DoubleGaussian` and `LogNormal`. Users can also utilise outputs from population synthesis simulations to generate their own populations and define cosmological parameters, such as the Hubble constant $H_0$, the CMB temperature $T_{\mathrm{CMB}}$, etc., to specify their Universe.

The `ifo` package provides core functionality for generating either zero-noise or coloured Gaussian noise given a noise power spectral density (PSD). It implements current and future ground-based GW detectors, detailing their locations, orientations, and various noise PSDs of existing and future instruments. Users can also implement custom GW detectors akin to `Bilby` (Ashton et al. 2019). Additionally, this package allows users to introduce data gaps, enabling the simulation of detector downtimes. This is important, as it creates a more realistic scenario, reflecting the potential for missing signals or having signals that are only partially present. By accounting for detector downtimes and data gaps, one can better understand the impact of these factors on gravitational wave detection and analysis, thereby improving the robustness of signal detection and parameter estimation methodologies.

Finally, the `inject` module provides essential functionalities for *injecting* or adding simulated GW signals into the data. It supports all standard waveform approximants available via the `lalsimulation` package (LIGO Scientific Collaboration et al. 2018) and/or those made available via PYCBC's waveform plugin.

Future updates will expand this module to include the capability to add non-Gaussian transients, Supernova (SNe) signals, and other GW transients, thereby making the network output more closely "mock" the real data.

### 2.3. *Executables*

To facilitate usability, we developed three key executables using the aforementioned packages: `gwforge_population`, `gwforge_noise`, and `gwforge_inject`. Each executable operates based on a configuration file tailored to its specific function. Additionally, the `gwforge_workflow` executable integrates all three tools and utilises the high-throughput computing framework HTCondor. This integration significantly accelerates the data generation process and simplifies user interaction by managing all ancillary tasks automatically. The following section provides an explicit example of using these executables.

## 3. SIMULATING A DAY'S WORTH OF MOCK DATA

### 3.1. *Background*

The observed GW strain $s(t \mid \boldsymbol{\theta}, I)$ at a detector $I$ can be expressed as:

$$s(t \mid \boldsymbol{\theta}, I) = \frac{1}{D_L} \mathbb{R} \left[ F^I h \right] \qquad (1)$$

where $\boldsymbol{\theta}$ is a vector representing the source's properties, $D_L$ is the luminosity distance to the source, $\mathbb{R}$ denotes the real part, and

$$F = F_+^I + i F_\times^I$$

is the antenna response function that depends on the sky location $(\alpha, \delta)$ and the polarization angle $(\psi)$. The term $h$ represents the complex binary waveform on a sphere. This waveform can be decomposed as a sum of spin-weighted spherical harmonic modes $h_{\ell m}$, so that the waveform along any direction $(\iota, \varphi)$ in the binary's source frame is given by:

$$h = \sum_{\ell \geq 2} \sum_{m=-\ell}^{\ell} {}^{-2}Y_{\ell,m}(\iota, \varphi) h_{\ell m}(t \mid \boldsymbol{\Xi}) \qquad (2)$$

Here, ${}^{-2}Y_{\ell,m}(\iota, \varphi)$ are the spin $-2$ weighted spherical harmonics, and $(\iota, \varphi)$ represent the binary's inclination and azimuth, respectively. The vector $\boldsymbol{\Xi}$ denotes

the binary's intrinsic parameters whose dimensionality depends on the binary type. For example, in quasi-spherical binary black holes (BBHs), $\Xi$ includes the two component masses $m_i$ and the six spin degrees of freedom $\boldsymbol{\chi}_i$. In contrast, for quasi-circular or non-precessing binary neutron stars (BNSs), $\Xi$ represents the component masses $m_i$, the tidal parameters $\Lambda_i$ and the aligned spin components $\boldsymbol{\chi}_i \cdot \hat{L}$, with $\boldsymbol{L}$ being the binary's orbital angular momentum.

Since the source's total merger rate and redshift distribution determine the number of signals in a given simulated dataset, `gwforge` begins by first estimating the average time interval $\langle \Delta t \rangle$ between two adjacent signals of the same type given the source population and the cosmological parameters. It assumes that all CBC systems are formed through isolated formation channels involving a common envelope phase. This allows it to derive the redshift distribution of CBCs in the source frame as follows (Zhu et al. 2021; Wu & Nitz 2023):

$$
\begin{aligned}
\mathcal{R}(z) &\propto \int_{\tau_{\min}}^{\infty} \mathcal{R}_*[z_f(z,\tau)]P(\tau)d\tau \\
&\propto \int_z^{\infty} \mathcal{R}_*(z_f)P[\tau(z,z_f)]\frac{dt(z_f)}{dz_f}\,dz_f \ .
\end{aligned}
\tag{3}
$$

Here, $\mathcal{R}_*$ is the cosmological star formation rate density, $P(\tau)$ is the probability density function of the delay time, $z_f$ is the redshift at which the stellar binary forms, $z$ is the redshift at which the compact binary merges, $\tau = t(z) - t(z_f)$ is the delay time and $t(z)$ is the lookback time at redshift $z$. The proportionality constant is defined such that $\mathcal{R}(z=0) = \mathcal{R}_0$ where $\mathcal{R}_0$ is the local merger rate density of the CBC source.

The lookback time,

$$
t(z) = \frac{1}{H_0} \int_z^{\infty} \frac{dz}{(1+z)\sqrt{\Omega_\Lambda + \Omega_m(1+z)^3}},
\tag{4}
$$

depends on the Hubble constant, $H_0$, the dark matter, $\Omega_\Lambda$ and matter density, $\Omega_m$. All these cosmological parameters, along with the star formation rate, are ad-justable by the user, allowing them to simulate their own Universe. However, `gwforge` currently only implements $P(\tau) \propto 1/\tau$.

Given this, the merger rate per redshift bin in the detector frame is then given by (Regimbau et al. 2012):

$$
\frac{dR}{dz} = \frac{\mathcal{R}}{1+z}\frac{dV(z)}{dz},
\tag{5}
$$

where the comoving volume element is given as:

$$
\frac{dV(z)}{dz} = \frac{c}{H_0}\frac{4\pi D_L^2}{(1+z)^2\sqrt{\Omega_\Lambda + \Omega_m(1+z)^3}} \ .
\tag{6}
$$

Here, $c$ is the light speed, and $D_L$ is the luminosity distance to the source defined as:

$$
D_L = \frac{c(1+z)}{H_0}\int_0^z \frac{dz'}{\sqrt{\Omega_\Lambda + \Omega_m(1+z')^3}}
\tag{7}
$$

The $1/(1+z)$ factor in Eq. (5) accounts for time dilation.

`gwforge` obtains $\langle \Delta t \rangle$ as follows:

$$
\langle \Delta t \rangle = 1/\left( \int_0^{z_{\max}} \frac{dR}{dz}dz \right) \ .
\tag{8}
$$

where $z_{\max}$ is the maximum redshift used in the simulation. Based on $\langle \Delta t \rangle$ and the total analysis time, $T_a$ of the network, `gwforge` determines the expected number of signals, $N = T_a/\langle \Delta t \rangle$, and correspondingly draws the binary parameters from the provided population models.

Below, we discuss an example to build a mock catalogue based on our current understanding of BBH binary population distribution.

### 3.2. *Simulating the mock GW catalogue*

To create a mock BBH catalogue using `gwforge`, one must first define a configuration file like the one provided below:

```
1  [Redshift]
2  redshift-model = MadauDickinson
3  redshift-parameters = {'gamma': 2.7, 'kappa': 5.6, 'z_peak': 1.9}
4  local-merger-rate-density = 22
5  maximum-redshift = 30
6  ; custom cosmology
7  cosmology = custom
8  H0 = 67.7
9  Om0 = 0.31
10 Ode0 = 0.69
11 Tcmb0 = 2.735
12 ; analysis start time
13 gps-start-time = 1893024018
14
15 [Mass]
16 mass-model = PowerLaw+Peak
```

```
17  mass-parameters = {'alpha':3.37, 'beta': 0.76, 'delta_m':5.23,  'mmin':4.89, 'mmax':88.81, 'lam':0.04, 'mpp':
        33.60, 'sigpp':4.59}
18
19  [Spin]
20  spin-model = default
21  spin-parameters = {'mu_chi':0.26, 'sigma_squared_chi':0.02, 'sigma_t':0.87, 'xi_spin':0.76}
22
23  [Extrinsic]
```

Within the [Redshift] section, users must specify the redshift evolution model, local merger rate density in /Gpc$^3$/yr, analysis start time (in GPS time), and the maximum redshift. Currently, gwforge supports two different redshift evolution models: the power-law redshift evolution model and the other that convolves the Madau-Dickinson star-formation rate with an inverse time-delay model to determine the CBC's redshift evolution model (Fishbach et al. 2018). Users can define custom cosmological and redshift parameters; otherwise, default values from Aghanim et al. (2020) and Madau-Dickinson parameters are used (Madau & Dickinson 2014).

Similarly, the [Mass] and [Spin] sections provide options for various phenomenological mass and spin distribution models, as detailed in Chandra (2024b). Besides predefined models, gwforge can utilize outputs from population-synthesis codes, creating interpolated distribution functions from variable and associated probability arrays, enabling sampling from simulated distributions.

Similarly, the [Mass] and [Spin] sections offer a selection of phenomenological mass and spin distribution models, as documented in Chandra (2024b). The

[Extrinsic] section deals with the *other* extrinsic parameters. Unless otherwise specified, gwforge employs the following default distribution choices for these parameters (See Table 2) for definitions of the symbols):

| variable | unit | distribution | minimum | maximum |
|---|---|---|---|---|
| $\alpha$ | rad. | uniform | 0 | $2\pi$ |
| $\delta$ | rad. | cos | $-\pi/2$ | $\pi/2$ |
| $\iota$ | rad. | sin | 0 | $\pi$ |
| $\psi$ | rad. | uniform | 0 | $\pi$ |
| $\phi$ | rad. | uniform | 0 | $2\pi$ |

**Table 1.** The default distribution functions for the sky location parameters, $(\alpha, \delta)$, inclination, $\iota$, polarisation angle $\psi$ and azimuth $\phi$.

Finally, if the binary contains a NS or a pair of NSs, gwforge can set the tidal parameters $\Lambda_i$ based on an Equation of State (EoS). This necessitates a pre-shipped ASCII table, examples of which can be found at Chandra (2024a). Additional configuration file examples are also provided at the same location.

Once the configuration file is defined, the next step is to execute:

```
1    gwforge_population --config-file bbh.ini --output-file bbh.h5
```

to create the mock BBH catalogue and store as in an hdf5 file.

### 3.3. *Mock noise generation*

After generating the mock GW catalogue, the next step is to define the detector network and simulate their noise. This can be achieved by creating a configuration file, for example, xg.ini, as shown below:

```
1  [IFOS]
2  detectors = ['CE20', 'CE40', 'ET']
3  sampling-frequency = 8192
4  noise = gaussian
```

and executing:

```
1    gwforge_noise --config-file xg.ini --output-directory output/data --gps-start-time 1895616018 --gps-end-time
        1895656978
```

This initialises a three-detector network consisting of two L-shaped CE observatories at two fiducial locations: CE40 off the coast of Washington State and CE20 off the coast of Texas, along with an underground triangular ET located in Sardinia, Italy (Evans et al. 2023; Gupta et al. 2023). The simulated noise thus produced will be Gaussian coloured by the detector noise PSD, with data sampled at 8192 Hz over approximately one day. The data will be stored as HDF5 files in the output/data directory, named in the format IFO-GPS-TIME.h5, with channel names IFO:INJ. To simulate zero-noise realisations, the user has to set the flag noise = zero.

gwforge also includes the two LIGO detectors in the US (Aasi et al. 2015), Virgo in PISA (Acernese et al. 2015), LIGO-Aundha in India (Iyer et al. 2011) and the KAGRA detector in Japan (Aso et al. 2013). It is also possible to define new detectors characterised by their geometry, location and frequency response. This feature is particularly useful for developing the science case for new proposals and optimising the design and placement of new detectors, such as placing the ET observatory in the Netherlands or building a pair of ET observatories at two different locations (Branchesi et al. 2023).

### 3.4. *Mock data generation*

The final step involves injecting the simulated GW signals into the network data. Similar to the previous steps, this requires a configuration file, for example, inject-bbh.ini, as shown below:

```
1  [IFOS]
2  detectors = ['CE20', 'CE40', 'ET']
3  channel-dict = {'CE20':'CE20:INJ', 'CE40':'CE40:INJ', 'ET':'ET:INJ'}
4  sampling-frequency = 8192
5  minimum-frequency = 6
6
7  [Injections]
8  injection-file = bbh.h5
9  injection-type = bbh
10 waveform-approximant = IMRPhenomXO4a
```

As with the noise generation step, the [IFOS] section requires specification of the detector network and sampling frequency. Additionally, this section must include the minimum frequency cut-off for signal generation and the channel names for the frame files. If not specified, gwforge assumes that the reference frequency for measuring the spin angles is the same as the minimum frequency used for signal generation.

The [Injections] section should contain the following keys: injection-file, which points to the file containing the mock BBH catalogue (e.g., bbh.h5); injection-type, which specifies the type of injection being made; and waveform-approximant, which indicates the waveform model to use for signal generation, with IMRPhenomXO4a being an example (Thompson et al. 2024). Currently, gwforge supports all waveform approximants available via the lalsimulation package (LIGO Scientific Collaboration et al. 2018). To use waveforms beyond those available in lalsimulation, a new plugin package must be created to advertise the new waveform model to PyCBC for waveform generation (Usman et al. 2016).

To inject the signal waveforms into the generated data over the specified GPS time interval, the user needs to execute the following command:
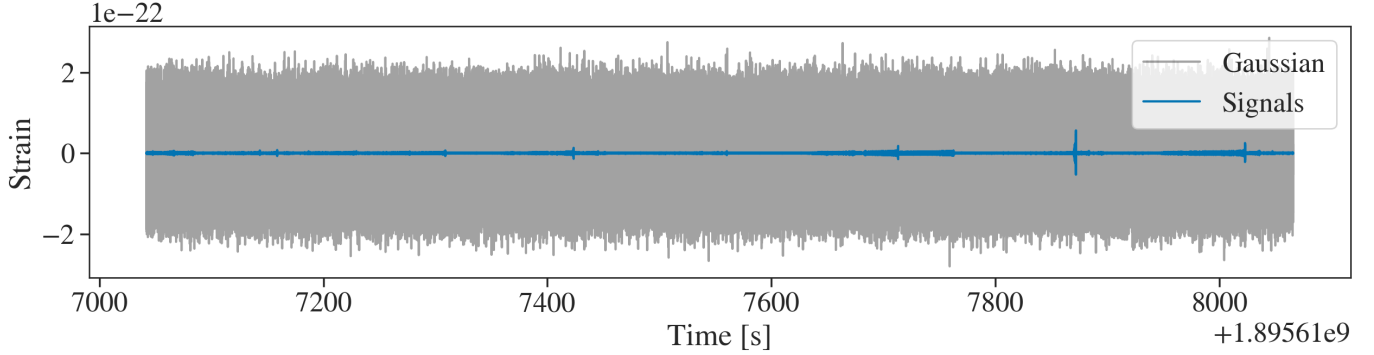
```
1  gwforge_inject --config-file forged-data/inject-bbh.ini --data-directory /output/data --gps-start-time 1895616018
       --gps-end-time 1895656978
```

This command injects the signal waveforms into the generated noise over the specified GPS time interval, creating the mock data for further study.

### 3.5. *Using gwforge_workflow*

Since the data generation process can be computationally expensive and time-consuming, users are encour-

**Figure 1.** A representative section of data generated using `gwforge`. The grey shows the Gaussian noise while the blue represents the sum of all GW signals, namely from BNS, BHNS and BBH.

aged to take advantage of `gwforge_workflow`, which leverages the high-throughput computing framework HTCondor. This significantly accelerates the data generation process by abstracting all other housekeeping logic away from the user. Once the mock catalogues are generated and the different configuration files are created, the following commands can be executed:

```
1  # Activate Conda environment
2  conda activate gwforge-test || { echo "Failed to activate Conda environment." >&2; exit 1; }
3
4  # Set output directory
5  output_directory=forged-data
6
7  # Workflow submission script
8  gwforge_workflow \
9      --gps-start-time 1895616018 \
10      --gps-end-time  1895702418 \
11      --output-directory "${output_directory}/output" \
12      --noise-configuration-file "${output_directory}/xg.ini" \
13      --bbh-configuration-file "${output_directory}/bbh-inject.ini" \
14      --bns-configuration-file "${output_directory}/bns.ini" \
15      --nsbh-configuration-file "${output_directory}/nsbh.ini" \
16      --workflow-name work \
17      --submit-now
```

This will create an HTCondor meta-scheduler to manage dependencies between jobs and systematically parallelize the tasks, accelerating the mock data generation process. Fig 1 shows 1024s of simulated data when assuming Gaussian noise, including signals from Population-A (See Sec. 4.1 for details). As can be seen, the data will never be "signal-free".
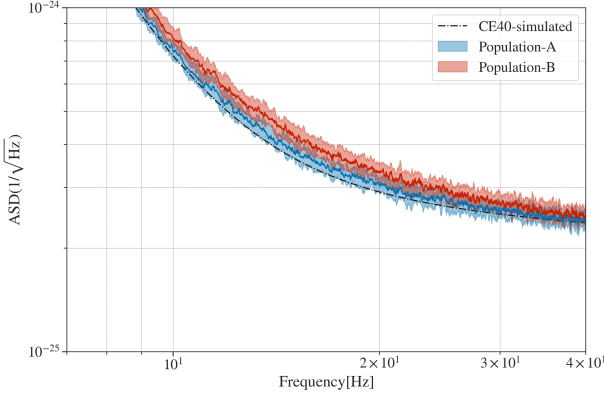
## 4. EXAMPLE USAGE OF THE MOCK DATA

### 4.1. *Foreground Noise*
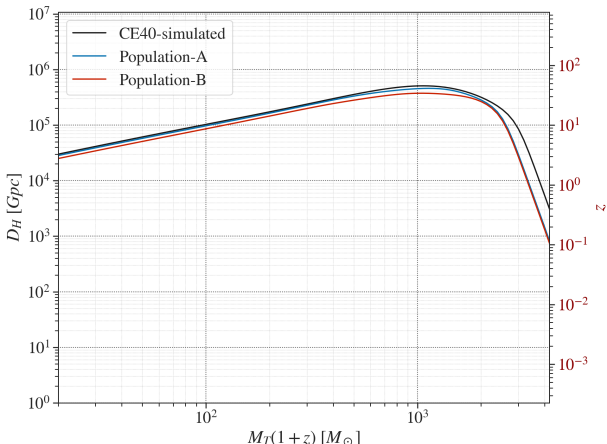
The increased bandwidth of XG detectors will allow low-mass CBC signals to remain within the detector's sensitive bandwidth for hours. Consequently, multiple signals will simultaneously appear in the data stream, the number of which will depend on the sources' astrophysical merger rate density. Characterised by their rapid frequency evolution, these signals will predominantly overlap at low frequencies and "separate" as they approach merger. Therefore, current modelled detection techniques can identify and measure their merger time to $\mathcal{O}(10ms)$ accuracy (Relton et al. 2022). As a result, unlike in LISA, where overlapping signals lead to source confusion, these signals will be resolvable and only contribute to *foreground noise*.

However, as the number of overlapping signals per time-frequency bin is small, their combined contribution won't obey the central limit theorem. Therefore, the data cannot be assumed to follow a wide-sense stationary Gaussian process — an assumption critical to the currently used noise PSD estimation technique such as the Welch averaging (Welch 1967; Allen et al. 2012) and the BayesLine method (Littenberg & Cornish 2015; Cornish & Littenberg 2015; Cornish et al. 2021). As a result, using these techniques without modification can result in biased PSD estimates. Such a deviation can introduce systematic biases in parameter inference and reduce CBC detectability.

**Figure 2.** Comparison of Welch ASD estimates for different realizations of 512 seconds of CE40 mock data. The black dotted line represents the ideal CE40 design sensitivity curve. The red curve indicates the estimate when the noise includes signals from population A, while the blue curve represents the estimate when the noise includes signals from population B. Both the red and blue curves include a 90% confidence band. The comparison demonstrates that depending on the number of signals, the ASD estimate can deviate from the expected noise ASD at 15Hz.



**Figure 3.** Comparison of horizon distance reach when using the median Welch ASD estimates. The black dotted line represents the ideal CE40 design sensitivity curve. The red curve indicates the estimate when the noise includes signals from population A, while the blue curve represents the estimate when the noise includes signals from population B. The comparison shows that depending on the number of signals, the horizon distance of a XG detector can be affected, especially for BBHs with a high detector frame (redshifted) total mass.

To demonstrate this, we simulate multiple realisations of 512s mock CE40 data using the `gwforge` package and estimate the noise PSD using the Welch method. Mathematically, this method assumes the data to be wide-sense stationary and divides the discrete time domain data $d[j]$ into $K$ overlapping segments $d_k[j]$ of length

$L$, each windowed by $w[j]$ which for our purpose, is the Hann truncation function. The discrete Fourier transform $\tilde{d}_k[i]$ of each windowed segment is computed using an FFT routine, and the periodogram $P_k[i]$ is obtained as

$$P_k[i] = \frac{1}{U}|\tilde{d}_k[i]|^2,$$

where $U = \sum_{n=0}^{L-1} w[j]^2$. We, following Allen et al. (2012), use mean-median averaging of the periodograms over all segments to obtain the final PSD estimate. This approach significantly reduces the variance of the spectral estimate due to glitches, thereby providing a more accurate representation of the data's power distribution across frequencies.

We assume two different source populations — population-A quantified by BNS and BHNS merger rate density of $\mathcal{R}^A_{BNS} = 320/\text{Gpc}^3/\text{yr}$, $\mathcal{R}^A_{BHNS} = 90/\text{Gpc}^3/\text{yr}$ respectively and population-B with merger-rate density of $\mathcal{R}^B_{BNS} = 1700/\text{Gpc}^3/\text{yr}$, $\mathcal{R}^B_{BHNS} = 200/\text{Gpc}^3/\text{yr}$ (LVK 2023, 2024). While overlapping BBH signals will lead to larger foreground noise, their lower local merger rate and shorter duration in the detector band suggest that they will rarely contribute to the foreground noise. We therefore use $\mathcal{R}_{BBH} = 30/\text{Gpc}^3/\text{yr}$ in both the cases.

Fig. 2 shows the simulated and the estimated CE40 ASD, with the latter obtained using the Welch method. It is estimated by dividing multiple-realisation of 512s of data into 16s subsegments and 50% overlap, akin to that used in a PyCBC search. Consistent with previous works (Wu & Nitz 2023; Evans et al. 2021), we find that the deviation is mainly concentrated between 6-30Hz, reaching $\gtrsim$ 10% at 15Hz for the upper merger rate. This can reduce the detectability of BBHs with a high detector frame (redshifted) total mass, as shown in Fig. 3. In particular, depending on the binary's detector frame mass, the horizon distance [1] loss to systems with $M_T(1+z) \gtrsim 1000 M_\odot$ can be $\gtrsim$ 15%. Similar to the Welch estimate, the median BayesLine output, which is widely used in GW PE, will also show a deviation, unless a joint spectral and signal estimate is performed with precision (see Appendix A for a discussion).

### 4.2. *Bright-siren cosmology*

GW signals from CBC sources can be used as probes for cosmic expansion (Schutz 1986). The luminosity distance, $D_L$ to a CBC can be directly estimated using the

---

[1] The horizon distance, $D_H$, for our case, is the farthest luminosity distance to which we can confidently detect an optimally oriented, located, non-spinning symmetric mass BBH assuming an optimal signal-to-noise ratio (SNR) threshold of 8.

**Table 2.** True value for the parameters used for the simulated IMBH binary. The values are inspired by the maximum likelihood values of GW190521 as inferred by Islam et al. (2023).
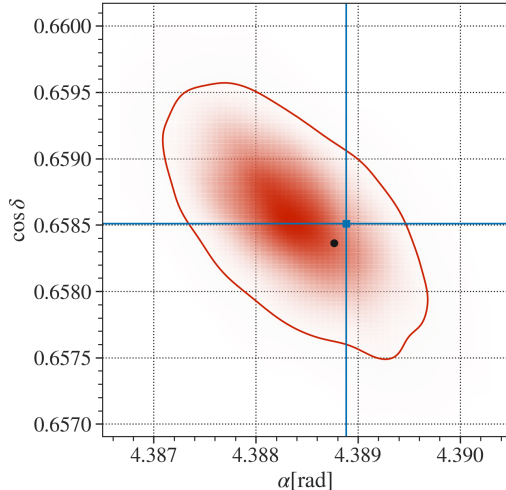
| Parameter | Symbol | Value |
|---|---|---|
| Mass ratio | $q$ | 0.95 |
| Detector-frame total mass | $M_T(1+z)$ | $273.83 M_\odot$ |
| Primary spin magnitude | $\chi_1$ | 0.83 |
| Secondary spin magnitude | $\chi_2$ | 0.96 |
| Primary tilt [a] | $\theta_1$ | 1.59 |
| Secondary tilt | $\theta_2$ | 1.96 |
| Azimuthal inter-spin angle | $\phi_{12}$ | 0.23 |
| Azimuthal precession cone angle | $\phi_{JL}$ | 0.36 |
| Effective aligned spin | $\chi_{\rm eff}$ | -0.19 |
| Effective precessing spin | $\chi_p$ | 0.83 |
| Coalescence phase | $\phi$ | 1.06 |
| Polarization angle | $\psi$ | 1.28 |
| Coalescence GPS time | $t_c$ | 1242442967.43s |
| Right ascension | $\alpha$ | 4.39 |
| Declination | $\delta$ | 0.85 |
| Redshift | $z$ | 0.76 |
| Inclination angle | $\theta_{JN}$ | 2.09 |
| Hubble constant | $H_0$ | 67.7km/s/Mpc |
| Matter density of Universe | $\Omega_m$ | 0.31 |

GW waveform $s(t \mid \boldsymbol{\theta}) \propto 1/D_L$ without needing external distance calibrators (Cutler & Flanagan 1994). If the CBC's cosmological redshift, $z$, can be estimated by other means, then one can infer the local expansion rate, $H_0$ and other cosmological parameters (Holz & Hughes 2005; Nissanke et al. 2010), such as the fractional energy density of dark energy, $\Omega_\Lambda$ and dark matter, $\Omega_m$. For example, observing the electromagnetic (EM) counterparts from GW170817 allowed us to identify the source's host galaxy, NGC 4993, enabling the first direct measurement of $H_0$ using GWs (Abbott et al. 2017).

Another promising EM-bright CBC source is BBHs mergers occurring in gas-rich environments such as active galactic nuclei (AGN) disks (McKernan et al. 2014; Bartos et al. 2017; McKernan et al. 2019; Graham et al. 2020). BBHs in such environments can efficiently merge due to gas torques and dynamical encounters, potentially producing detectable EM radiation during or after the merger. Such detection is feasible even against bright AGN disks, provided the disks are thin and relatively low in luminosity or if the merger remnant is ejected from the optically thick midplane and undergoes super-Eddington accretion.

XG detectors promise to play a pivotal role in inferring cosmological parameters (Chen et al. 2024; Corsi et al. 2024). To demonstrate how the mock data can be used to perform bright-siren cosmology, we analyse 8s of XG detector data segment containing a GW190521-like binary that coincides with an EM counterpart with $\{\alpha_{\rm em}, \delta_{\rm em}, z_{\rm em}\}$ same as the simulated signal. The

data includes Gaussian noise and Population-A binaries, as introduced in the previous subsection. The binary and cosmological parameters used for the analysis are tabulated in Table 2. We use the Bayesian PE library `Bilby` (Ashton et al. 2019), waveform model `NRSur7dq4` (Varma et al. 2019) and off-the-shelf dynamic nested sampler `dynesty` (Speagle 2020). We use the same waveform model for injection and recovery to prevent waveform systematics. Consistent with the mock data generation set-up, we use a minimum-frequency cutoff of $f_{\min} = 6$Hz and perform a flare-unrestricted PE with standard priors (Abbott et al. 2020) and PSD calculated using the Welch method.
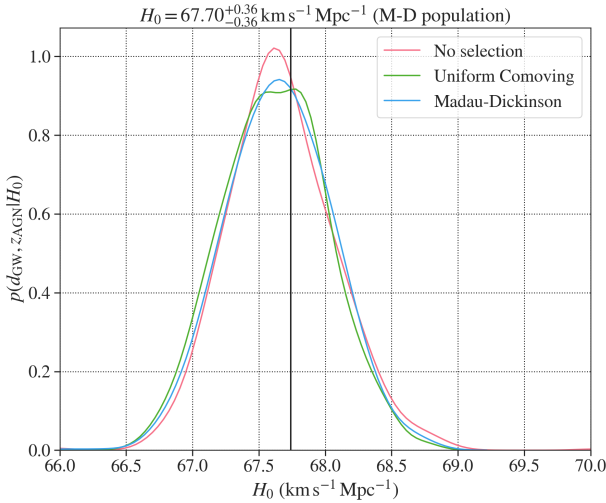


**Figure 4.** Posterior probability density for the sky-location of the GW190521-like signal in XG network data. The blue square shows the sky location of the simulated binary, and the black dot shows the maximum likelihood sky location

Fig. 4 shows the posterior probability distributions for the sky-location of simulated binary. As can be seen, the sky location of the flare and the GW signal are consistent. In fact, the odds of a common source hypothesis $C$, against a random coincidence, $\mathcal{O}_{C/R} > 2 \times 10^7$, if we assume the prior odds, $\pi_{C/R}$, to be unity.

Having confirmed such an association, we use the obtained posterior samples to infer $H_0$ (Abbott et al. 2017; Chen et al. 2022) given the GW and EM datasets, $d_{\rm gw}$ and $d_{\rm em}$:

$$
\begin{aligned}
p(H_0 \mid d_{\rm em}, d_{\rm gw}) \propto{}& \pi(H_0) \\
&\times \mathcal{L}\left(d_{\rm gw} \mid \alpha_{\rm em}, \delta_{\rm em}, D_L(z_{\rm em} \mid H_0)\right) \\
&\times \frac{\pi_{\rm pop}(z_{\rm em} \mid H_0)}{\beta(H_0)} \,.
\end{aligned}
\tag{9}
$$

$H_0 = 67.70^{+0.36}_{-0.36}\,\mathrm{km\,s^{-1}\,Mpc^{-1}}$ (M-D population)
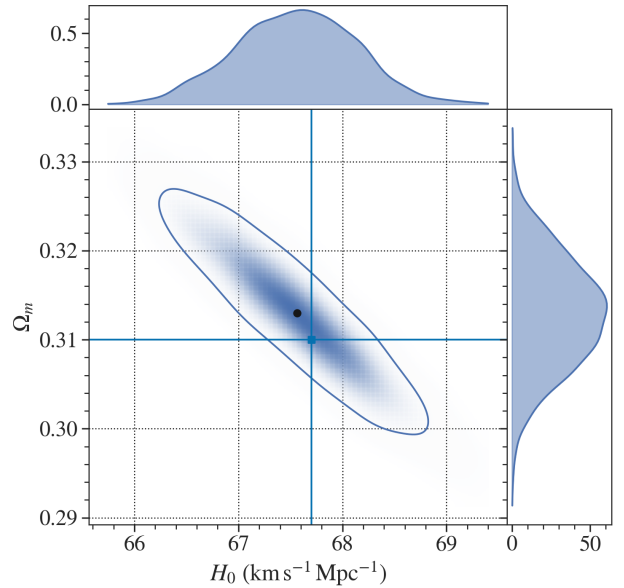
**Figure 5.** The posterior pdf of $H_0$ for the event under the assumption of flat $\Lambda$CDM cosmology and physical matter constraints from Aghanim et al. (2020). The red curve assumes no selection effect, while the green and blue curve assumes that the underlying BBH population follows a Uniform in Comoving volume and star formation rate as modelled by Madau & Dickinson (2014) respectively.

Here $\pi(H_0)$ is the prior on $H_0$, $\mathcal{L}$ is the marginalised GW likelihood function evaluated at the distance and sky location of the electromagnetic source, $\pi_{\mathrm{pop}}(z_{\mathrm{em}} \mid H_0)$ is the assumed redshift distribution of the binary population and $\beta(H_0)$ is the fraction of binary population that will be simultaneously detected in GW and EM window.

Fig 5 shows our results, assuming a flat $\Lambda$CDM cosmology and matter constraints from Aghanim et al. (2020). We assume $\pi(H_0) = \mathcal{U}(35, 140)$km/s/Mpc and consider two redshift distribution models: one that assumes that BBH merger rate is constant up to redshift $z = 10$ and the other that follows the Madau-Dickinson star-formation rate used to simulate the binary population. For both cases, we first estimate $\beta(H_0)$ following Farr & Gair (2018) and then infer $H_0$ to be $67.7^{+0.36}_{-0.36}$km/s/Mpc at 68% CI, thereby being consistent with the value used in simulating the binary population. It shows that if the uncertainty in luminosity distance and the counterpart redshift measurement is small, XG EM-bright sources can precisely measure $H_0$, irrespective of the underlying population distribution assumption.

In Fig 6, we present the measurements of $\Omega_m$ and $H_0$, when using flat priors in the range $H_0 = [35, 140]$km/s/Mpc, $\Omega_m = [0, 1]$ and assuming $\Lambda$CDM cosmology. For this, we obtain the joint posterior on



**Figure 6.** The joint posterior pdf of $H_0$ and $\Omega_m$ for the event using uniform priors for all the parameters in a flat $\Lambda$CDM ($w = -1$) cosmology. The contour encloses 90% CI. The blue square shows the cosmological parameters used for the simulations, while the black dot shows the maximum likelihood sky location.

$(H_0, \Omega_m)$ by modifying Eq. (9) to the following:
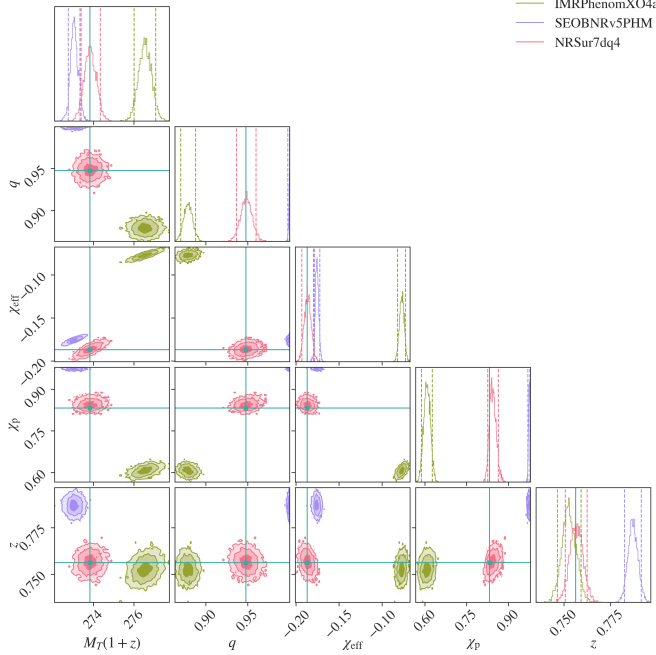
$$
\begin{aligned}
p(H_0, \Omega_m \mid d_{\mathrm{em}}, d_{\mathrm{gw}}) \propto\ & \pi(H_0, \Omega_m) \\
& \times \mathcal{L}\left(d_{\mathrm{gw}} \mid \alpha_{\mathrm{em}}, \delta_{\mathrm{em}}, D_L(z_{\mathrm{em}} \mid H_0, \Omega_m)\right) \\
& \times \frac{\pi_{\mathrm{pop}}(z_{\mathrm{em}} \mid H_0, \Omega_m)}{\beta(H_0, \Omega_m)}\ .
\end{aligned}
\tag{10}
$$

Consistent with Fig. 5, the maximum likelihood point is close to the true value. However, as expected, the posterior for $H_0$ is broader.

### 4.3. *PE biases due to waveform systematics*

GWs from CBCs carry characteristic information about the astrophysical properties of compact objects, such as their masses and spins. A significant challenge in inferring these parameters is the systematic error introduced by the waveform approximants. If two waveform models, $\mathcal{W}_1$ and $\mathcal{W}_2$ do not agree for a particular choice of $\boldsymbol{\theta}$, i.e. $\delta h = h_1(t \mid \boldsymbol{\theta}, \mathcal{W}_1) - h_2(t \mid \boldsymbol{\theta}, \mathcal{W}_2) \nrightarrow 0$, then it can significantly skew PE outcomes. This is especially problematic if the difference exceeds the detector noise level.

More rigorously, if the two waveform models are not *faithful* up to a particular level determined by the signal's SNR, then the disagreement between the waveform models will lead to differences in PE outputs. This issue is particularly critical in XG era, where we anticipate observing over $10^5$ compact binary signals per year, few of

**Figure 7.** Comparison corner plot for the posteriors obtained for the redshifted total mass, mass ratio, effective aligned and precessing parameters and the redshift for the GW190521-like signal when using three different waveform approximants. The cyan lines correspond to the true values.

which can have a SNR greater than 100. Since the statistical uncertainty of parameter estimates decreases with an increase in SNR, the measurability of signal parameters can be significantly affected if the current waveform models are used, particularly when analysing high SNR events (Pürrer & Haster 2020; Dhani et al. 2024; Kapil et al. 2024). Consequently, it is crucial to understand how waveform systematics can lead to incongruous results.

While a detailed study is deferred to future work, we provide an illustrative example of using the simulated mock data to identify biases in PE due to waveform systematics. We note that these studies must be performed in zero-noise so that no systematics are introduced due to noise. Here, we give an example where the noise is Gaussian and includes population-A signals.

To this end, we re-analyse the mock data segment containing the GW190521-like `NRSur7dq4` signal with parameters tabulated in Table 2 with three different state-of-the-art waveform models, namely `NRSur7dq4`, `IMRPhenomXO4a` and `SEOBNRv5PHM` (Ramos-Buades et al. 2023). For each of these analyses, we use `Bilby`, employ standard priors and the standard likelihood function for GW transients (Finn 1992) and evaluate it from a fixed minimum frequency of $f_{\min} = 6$Hz identical to the reference frequency choice.

Fig. 7 shows a corner plot comparing a few binary parameters. As can be seen, depending on the waveform approximant, the recovered parameters can be significantly different from the injected value. This is because these waveform models differ in their construction; therefore, measurements relying on them can have systematic uncertainties. This has not been an issue for almost all second-generation GW candidates, as differences caused by different approximant choices have been lower than those induced by noise fluctuations. But for loud XG events, this can introduce significant biases as the statistical uncertainty of parameter estimates decreases with an increase in SNR (Kapil et al. 2024; Dhani et al. 2024). Standard approaches to account for modelling errors, such as combining posterior for analysis performed using different approximants to yield a joint posterior that is effectively marginalised over the uncertainty inherent in the waveform models, won't alone be able to account for the errors and biases that occur during the recovery of source parameters due to waveform modelling choices.

### 4.4. Other possible challenges

The data generated using `gwforge` can be used to address several other challenges, some of which are summarised below:

1. **Testing faster and more robust search and PE algorithms:** The XG detectors are expected to observe hundreds of thousands of binary signals annually. Developing optimal signal identification methods and rapid parameter estimation algorithms tailored to compact binary analysis will be essential for extracting science from the signal-rich dataset. In this context, the traditional requirement of achieving a $\gtrsim 5\sigma$ confidence level may no longer be necessary. Instead, search design requirements can be adapted to enable faster detection and PE algorithms can be developed and/or tuned for faster and more precise estimation of signal properties.

   Moreover, non-stationary noise due to glitches and foreground noise will necessitate a joint analysis of the signal of interest and the remaining data. In fact, current search techniques can be replaced by coherent Bayesian search algorithms that will allow for the identification of potential candidates, give rapid, fully coherent parameter estimates of the signal source, and assign astrophysical probabilities of the candidate events (Isi et al. 2018). The simulated datasets will allow the GW community to develop, test, and refine algorithms to meet these scientific objectives.

2. **Measurement of NS EoS:** GWs from binaries consisting of a pair of NS, or a NS and a Black hole (BH) can be used to measure the tidal deformability of NSs and constrain the nature of matter at supernuclear densities (Hinderer et al. 2010; Damour et al. 2012; Del Pozzo et al. 2013). Given that these effects appear in the fifth post-Newtonian order, this will be best measured for signals with SNR of order thousands, akin to those expected to be observed in XG era. The `gwforge` dataset will contain such signals depending on the initial conditions and can be used to verify how precisely and accurately one can measure the NS EoS. Further, it can be used to quantify any observed bias due to the foreground noise. Also, depending on the waveform model used, the post-inspiral portion of the signals may also be present in the simulated dataset which can be used to study how well we can constrain the presence of phase transitions at several times the nuclear densities (Radice et al. 2017; Most et al. 2019, 2020; Prakash et al. 2024).

3. **Testing rapid pre-merger sky localisation algorithms:** Low latency detection and pre-merger localisation of potential BNS signals, especially those within the reach of electromagnetic observatories, will be an important scientific goal for XG CBC algorithms as they can allow for a multiband understanding of BNSs. The `gwforge` dataset can be used to mimic online analysis. It will allow the community to combine multi-messenger observation of future mergers to more precisely determine the NS EoS and learn about the engine powering gamma-ray bursts, kilonovae and the formation of heavy elements.

4. **Estimate the strength of the stochastic background due to compact binary population:** The aggregate of all sources, particularly binary neutron stars will contribute to foreground noise which could interfere with the study or the establishment of upper limits on the cosmological GW background. Therefore, it is crucial to either remove or account for this foreground to measure the properties of a primordial background accurately. `gwforge` datasets will facilitate extensive testing of XG algorithms on large and realistic samples.

5. **Investigating Deviations from general relativity (GR) and False Violations:** `gwforge` allows injecting non-GR signals through a PyCBC plugin, enabling users to introduce and analyze these signals. This feature facilitates studies on the efficacy of conventional tests in detecting deviations from GR. Additionally, users can inject GR signals to investigate scenarios where tests of GR may fail. Such failures could arise due to waveform systematics, sub-optimal detector noise modelling, and various astrophysical aspects. By examining both non-GR and GR signals, `gwforge` dataset will allow us to perform mock tests of GR in XG era.

6. **Determining Merger Rates and Reconstructing the Underlying Distribution of Source Populations:** Given the anticipated high number of detections, utilizing current hierarchical Bayesian inference techniques to determine the population properties of a CBC type may become impractical. However, the sheer volume of signals allows for an alternative approach: multiplying the posteriors of individual events of a particular source type to infer population properties. The `gwforge` dataset will enable the validation of this hypothesis and facilitate the testing of faster and more accurate Bayesian inference techniques.

## 5. CONCLUSION

In the upcoming decades, XG detectors are expected to replace the current GW detection facilities. With longer baselines and new infrastructures, these detectors can make transformative discoveries across astronomy, physics and cosmology. However, the "richer" GW detector data will pose new computational, physical and astrophysical challenges, which may not be straightforward to mitigate.

For example, the sheer volume of signals will require developing novel signal identification and extraction algorithms. Non-stationarity due to foreground noise will pose additional challenges, especially in noise modelling, complicating subsequent analysis. Furthermore, detecting loud signals will necessitate the development of improved waveform models to achieve unprecedented precision in parameter estimations and avoid false indications of deviations from GR.
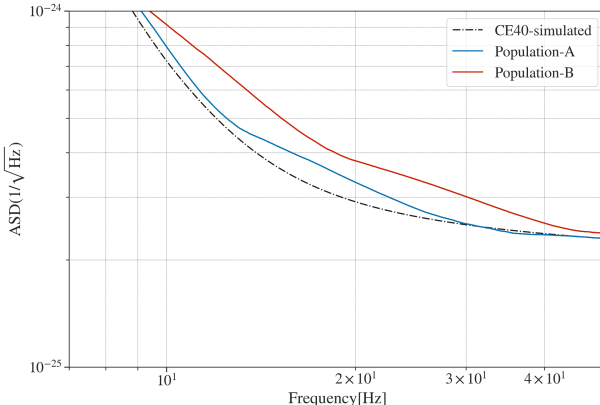
To simulate these challenges, we introduce `gwforge`, a user-friendly and lightweight Python package designed to generate mock data for XG detectors. Through various data simulation examples, we demonstrate the capabilities of `gwforge`. These examples include examining foreground noise from overlapping signals with intersecting time-frequency tracks, demonstrating the potential of bright sirens for $H_0$ measurement, and discussing parameter estimation biases due to waveform systematics. We also highlight a few potential challenges that

12

can be addressed using the simulated dataset. These demonstrations underscore the potential applications of `gwforge` in supporting the development of new analysis methods and preparing the scientific community for the next era of gravitational wave astronomy.

ACKNOWLEDGEMENTS

The author thanks B.S. Sathyaprakash, Ian Harry, Rossella Gamba and Ish Gupta for their insightful comments and valuable suggestions. He extends special thanks to Sophie Hourihane for her assistance with BayesLine. Heartfelt appreciation is also given to Lorine Talhaoui, Tobias Forge, Papa Nihil, and N. Ghouls for their continuous inspiration throughout the development of this work.

The author acknowledges the generous support of the National Science Foundation (NSF) through grant PHY-2207638. He is also grateful for the computational resources provided by the Gwave (PSU) cluster, which were essential for the numerical work conducted in this research.

The `gwforge` package extensively utilises the following `gw` packages: `Bilby` (Ashton et al. 2019), Py-CBC (Usman et al. 2016), `gwpy` (Macleod et al. 2021), and `Lalsuite` (LIGO Scientific Collaboration et al. 2018). Furthermore, various PYTHON packages such as `numpy` (Harris et al. 2020), `matplotlib` (Hunter 2007), `corner` (Foreman-Mackey 2016), and `seaborn` (Waskom 2021) are used in this work.

APPENDIX



**Figure 8.** Comparison of BayesLine median ASD estimates of 512 seconds of CE40 mock data. The black dotted line represents the ideal CE40 design sensitivity curve. The red curve indicates the estimate when the noise includes signals from population A, while the blue curve represents the estimate when the noise includes signals from population B. The comparison demonstrates that depending on the number of signals, the ASD estimate can deviate significantly at lower frequencies from the expected noise.

## A. BAYESLINE PSD ESTIMATE

The Welch method for estimating noise power spectral density (PSD) generates an "off-source" noise PSD by median-averaging the spectral estimates of neighbouring data segments. However, it is not widely used in GW PE due to its sensitivity to non-Gaussian transients or "glitches". Moreover, even for wide-sense stationary Gaussian noise, the data whitened by the Welch method doesn't produce a $\mathcal{N}(0,1)$ distribution, leading to biased PE estimates (Talbot & Thrane 2020; Chatziioannou et al. 2019).

Hence, current LIGO-Virgo-Kagra Collaboration (LVK) analyses use the "on-source" Bayesian spectral estimates, such as those provided by the BAYESLINE algorithm (Littenberg & Cornish 2015; Cornish & Littenberg 2015; Cornish et al. 2021). This method approximates the noise PSD by generating a parameterised fit involving a combination of splines and Lorentzians. This has yielded unbiased and statistically consistent results, with whitened residuals that follow a $\mathcal{N}(0,1)$ distribution.

Furthermore, this methodology, originally developed for joint spectral and signal inference, will be indispensable in the upcoming XG era, where no signal-free off-source data will be available. However, current LVK analysis uses sequential modelling, which may lead to notable discrepancies from joint analyses as detector sensitivities improve. This discrepancy becomes more pronounced, particularly for ground-based XG detectors, as the sum of foreground noise won't follow a Gaussian distribution.

To illustrate that, we re-compute the noise PSD of a 512s segment of data as discussed in Sec. 4.1 using the BAYESLINE algorithm. Fig. 8 shows our result. Like the Welch estimate, the foreground noise significantly affects noise characterisation at lower frequencies, with a more pronounced impact observed for population-B data, which assumes upper merger rates for BNS and BHNS systems. This can affect PE results, potentially broadening constraints on parameters like chirp mass ($\mathcal{M}_c$) and/or symmetric mass ratio ($\eta$) for longer signals while not significantly affecting the measurability of parameters appearing at higher post-Newtonian (PN) orders (see Johnson et al. (2024) for a possible way to mitigate this). However, this may substantially impact

binary parameter measurements for short-lived signals, such as IMBH binaries. A detailed investigation is deferred to future work.

## REFERENCES

2023, Phys. Rev. X, 13, 011048,
doi: 10.1103/PhysRevX.13.011048

2024. https://arxiv.org/abs/2404.04248

Aasi, J., et al. 2015, Class. Quant. Grav., 32, 074001,
doi: 10.1088/0264-9381/32/7/074001

Abbott, B. P., et al. 2017, Nature, 551, 85,
doi: 10.1038/nature24471

Abbott, R., et al. 2020, Phys. Rev. Lett., 125, 101102,
doi: 10.1103/PhysRevLett.125.101102

Acernese, F., et al. 2015, Class. Quant. Grav., 32, 024001,
doi: 10.1088/0264-9381/32/2/024001

Aghanim, N., et al. 2020, Astron. Astrophys., 641, A6,
doi: 10.1051/0004-6361/201833910

Allen, B., Anderson, W. G., Brady, P. R., Brown, D. A., &
Creighton, J. D. E. 2012, Phys. Rev. D, 85, 122006,
doi: 10.1103/PhysRevD.85.122006

Ashton, G., et al. 2019, Astrophys. J. Suppl., 241, 27,
doi: 10.3847/1538-4365/ab06fc

Aso, Y., Michimura, Y., Somiya, K., et al. 2013, Phys. Rev.
D, 88, 043007, doi: 10.1103/PhysRevD.88.043007

Bartos, I., Kocsis, B., Haiman, Z., & Márka, S. 2017,
Astrophys. J., 835, 165,
doi: 10.3847/1538-4357/835/2/165

Borhanian, S., & Sathyaprakash, B. S. 2022.
https://arxiv.org/abs/2202.11048

Branchesi, M., et al. 2023, JCAP, 07, 068,
doi: 10.1088/1475-7516/2023/07/068

Chandra, K. 2024a, GWForge: A lightweight code to
generate mock gravitational wave detector data,
https://github.com/koustavchandra/gwforge

—. 2024b, GWForge Documentation,
https://koustavchandra.github.io/gwforge/index.html

Chatziioannou, K., Haster, C.-J., Littenberg, T. B., et al.
2019, Phys. Rev. D, 100, 104004,
doi: 10.1103/PhysRevD.100.104004

Chen, H.-Y., Ezquiaga, J. M., & Gupta, I. 2024, Class.
Quant. Grav., 41, 125004, doi: 10.1088/1361-6382/ad424f

Chen, H.-Y., Haster, C.-J., Vitale, S., Farr, W. M., & Isi,
M. 2022, Mon. Not. Roy. Astron. Soc., 513, 2152,
doi: 10.1093/mnras/stac989

Cornish, N. J., & Littenberg, T. B. 2015, Class. Quant.
Grav., 32, 135012, doi: 10.1088/0264-9381/32/13/135012

Cornish, N. J., Littenberg, T. B., Bécsy, B., et al. 2021,
Phys. Rev. D, 103, 044006,
doi: 10.1103/PhysRevD.103.044006

Corsi, A., et al. 2024. https://arxiv.org/abs/2402.13445

Cutler, C., & Flanagan, E. E. 1994, Phys. Rev. D, 49, 2658,
doi: 10.1103/PhysRevD.49.2658

Damour, T., Nagar, A., & Villain, L. 2012, Phys. Rev. D,
85, 123007, doi: 10.1103/PhysRevD.85.123007

Del Pozzo, W., Li, T. G. F., Agathos, M., Van Den Broeck,
C., & Vitale, S. 2013, Phys. Rev. Lett., 111, 071101,
doi: 10.1103/PhysRevLett.111.071101

Dhani, A., Völkel, S., Buonanno, A., et al. 2024.
https://arxiv.org/abs/2404.05811

Evans, M., et al. 2021. https://arxiv.org/abs/2109.09882

—. 2023. https://arxiv.org/abs/2306.13745

Farr, W. M., & Gair, J. R. 2018, H0StatisticalLikelihood,
https://github.com/farr/H0StatisticalLikelihood

Finn, L. S. 1992, Phys. Rev. D, 46, 5236,
doi: 10.1103/PhysRevD.46.5236

Fishbach, M., Holz, D. E., & Farr, W. M. 2018, Astrophys.
J. Lett., 863, L41, doi: 10.3847/2041-8213/aad800

Foreman-Mackey, D. 2016, The Journal of Open Source
Software, 1, 24, doi: 10.21105/joss.00024

Graham, M. J., et al. 2020, Phys. Rev. Lett., 124, 251102,
doi: 10.1103/PhysRevLett.124.251102

Gupta, I., et al. 2023. https://arxiv.org/abs/2307.10421

Harris, C. R., Millman, K. J., van der Walt, S. J., et al.
2020, Nature, 585, 357, doi: 10.1038/s41586-020-2649-2

Hinderer, T., Lackey, B. D., Lang, R. N., & Read, J. S.
2010, Phys. Rev. D, 81, 123016,
doi: 10.1103/PhysRevD.81.123016

Holz, D. E., & Hughes, S. A. 2005, Astrophys. J., 629, 15,
doi: 10.1086/431341

Hu, Q., & Veitch, J. 2023, Astrophys. J., 945, 103,
doi: 10.3847/1538-4357/acbc18

Hunter, J. D. 2007, Computing In Science & Engineering,
9, 90

Isi, M., Smith, R., Vitale, S., et al. 2018, Phys. Rev. D, 98,
042007, doi: 10.1103/PhysRevD.98.042007

Islam, T., Vajpeyi, A., Shaik, F. H., et al. 2023.
https://arxiv.org/abs/2309.14473

Iyer, B. R., Souradeep, T., Unnikrishnan, C. S., et al. 2011,
LIGO-India, Proposal of the Consortium for Indian
Initiative in Gravitational-Wave Observations (IndIGO)

Johnson, A. D., Chatziioannou, K., & Farr, W. M. 2024,
Phys. Rev. D, 109, 084015,
doi: 10.1103/PhysRevD.109.084015

14

Kapil, V., Reali, L., Cotesta, R., & Berti, E. 2024, Phys. Rev. D, 109, 104043, doi: 10.1103/PhysRevD.109.104043

LIGO Scientific Collaboration, Virgo Collaboration, & KAGRA Collaboration. 2018, LVK Algorithm Library - LALSuite, Free software (GPL), doi: 10.7935/GT1W-FZ16

Littenberg, T. B., & Cornish, N. J. 2015, Phys. Rev. D, 91, 084034, doi: 10.1103/PhysRevD.91.084034

Macleod, D. M., Areeda, J. S., Coughlin, S. B., Massinger, T. J., & Urban, A. L. 2021, SoftwareX, 13, 100657, doi: 10.1016/j.softx.2021.100657

Madau, P., & Dickinson, M. 2014, Ann. Rev. Astron. Astrophys., 52, 415, doi: 10.1146/annurev-astro-081811-125615

Maggiore, M., et al. 2020, JCAP, 03, 050, doi: 10.1088/1475-7516/2020/03/050

McKernan, B., Ford, K. E. S., Kocsis, B., Lyra, W., & Winter, L. M. 2014, Mon. Not. Roy. Astron. Soc., 441, 900, doi: 10.1093/mnras/stu553

McKernan, B., Ford, K. E. S., Bartos, I., et al. 2019, Astrophys. J. Lett., 884, L50, doi: 10.3847/2041-8213/ab4886

Most, E. R., Jens Papenfort, L., Dexheimer, V., et al. 2020, Eur. Phys. J. A, 56, 59, doi: 10.1140/epja/s10050-020-00073-4

Most, E. R., Papenfort, L. J., Dexheimer, V., et al. 2019, Phys. Rev. Lett., 122, 061101, doi: 10.1103/PhysRevLett.122.061101

Nissanke, S., Holz, D. E., Hughes, S. A., Dalal, N., & Sievers, J. L. 2010, Astrophys. J., 725, 496, doi: 10.1088/0004-637X/725/1/496

Pizzati, E., Sachdev, S., Gupta, A., & Sathyaprakash, B. 2022, Phys. Rev. D, 105, 104016, doi: 10.1103/PhysRevD.105.104016

Prakash, A., Gupta, I., Breschi, M., et al. 2024, Phys. Rev. D, 109, 103008, doi: 10.1103/PhysRevD.109.103008

Punturo, M., et al. 2010, Class. Quant. Grav., 27, 194002, doi: 10.1088/0264-9381/27/19/194002

Pürrer, M., & Haster, C.-J. 2020, Phys. Rev. Res., 2, 023151, doi: 10.1103/PhysRevResearch.2.023151

Radice, D., Bernuzzi, S., Del Pozzo, W., Roberts, L. F., & Ott, C. D. 2017, Astrophys. J. Lett., 842, L10, doi: 10.3847/2041-8213/aa775f

Ramos-Buades, A., Buonanno, A., Estellés, H., et al. 2023, Phys. Rev. D, 108, 124037, doi: 10.1103/PhysRevD.108.124037

Regimbau, T., et al. 2012, Phys. Rev. D, 86, 122001, doi: 10.1103/PhysRevD.86.122001

Reitze, D., et al. 2019, Bull. Am. Astron. Soc., 51, 035. https://arxiv.org/abs/1907.04833

Relton, P., Virtuoso, A., Bini, S., et al. 2022, Phys. Rev. D, 106, 104045, doi: 10.1103/PhysRevD.106.104045

Schutz, B. F. 1986, Nature, 323, 310, doi: 10.1038/323310a0

Speagle, J. S. 2020, Mon. Not. Roy. Astron. Soc., 493, 3132, doi: 10.1093/mnras/staa278

Stevenson, S., Vigna-Gómez, A., Mandel, I., et al. 2017, Nature Commun., 8, 14906, doi: 10.1038/ncomms14906

Talbot, C., & Thrane, E. 2020, Phys. Rev. Res., 2, 043298, doi: 10.1103/PhysRevResearch.2.043298

Thompson, J. E., Hamilton, E., London, L., et al. 2024, Phys. Rev. D, 109, 063012, doi: 10.1103/PhysRevD.109.063012

Usman, S. A., et al. 2016, Class. Quant. Grav., 33, 215004, doi: 10.1088/0264-9381/33/21/215004

Varma, V., Field, S. E., Scheel, M. A., et al. 2019, Phys. Rev. Research., 1, 033015, doi: 10.1103/PhysRevResearch.1.033015

Vigna-Gómez, A., et al. 2018, Mon. Not. Roy. Astron. Soc., 481, 4009, doi: 10.1093/mnras/sty2463

Waskom, M. L. 2021, Journal of Open Source Software, 6, 3021, doi: 10.21105/joss.03021

Welch, P. 1967, IEEE Trans. Audio Electroacoust., 15, 70, doi: 10.1109/TAU.1967.1161901

Wu, S., & Nitz, A. H. 2023, Phys. Rev. D, 107, 063022, doi: 10.1103/PhysRevD.107.063022

Zhu, J.-P., et al. 2021, Astrophys. J., 917, 24, doi: 10.3847/1538-4357/abfe5e